



Defect-rich ZnO nanosheets of high surface area as an efficient visible-light photocatalyst



Jing Wang^{a,b,1}, Yi Xia^{a,1}, Yan Dong^b, Ruosong Chen^a, Lan Xiang^{a,*}, Sridhar Komarneni^{b,*}

^a Department of Chemical Engineering, Tsinghua University, Beijing 100084, China

^b Department of Ecosystem Science and Management and Materials Research Institute, Materials Research Laboratory, The Pennsylvania State University, University Park, PA 16802, USA

ARTICLE INFO

Article history:

Received 11 February 2016

Received in revised form 3 March 2016

Accepted 17 March 2016

Available online 18 March 2016

Keywords:

ZnO

Defect-rich

High surface area

Visible-light photocatalyst

Synergistic effect

ABSTRACT

A facile ultra-rapid solution method was developed to fabricate ZnO nanosheets with tunable BET surface area and rich oxygen-vacancy defects. The addition of $1 \text{ mol L}^{-1} \text{ Na}_2\text{SO}_4$ led to an increase of BET surface area of ZnO nanosheets from 6.7 to $34.5 \text{ m}^2/\text{g}$, through an electrostatic-controlled growth and self-assembly mechanism. Detailed analysis based on Raman scattering, room-temperature photoluminescence, X-ray photoelectron spectroscopy and electron spin resonance revealed that the as-prepared ZnO nanosheets were rich in oxygen-vacancies. Increased BET surface area led to a further increase of surface oxygen-vacancy concentration. The rich oxygen-vacancies promoted the visible-light absorption of the ZnO nanosheets, leading to high photocurrent responses and photocatalytic activities towards the degradation of rhodamine B (apparent rate constants, $k = 0.0179 \text{ min}^{-1}$) under visible-light illumination ($\lambda > 420 \text{ nm}$), about 13 and 11 times higher, respectively than that of ZnO nanoparticles with few oxygen defects. In addition, the high-surface-area ZnO nanosheets could be effectively hybridized with Ag_3PO_4 nanoparticles, resulting in a further enhancement of the visible-light photocatalytic performance ($k = 0.0421 \text{ min}^{-1}$). This increase in performance was attributed to the increased visible-light absorption as well as the energy level matching, the latter leading to efficient charge transfer between oxygen-vacancy-rich ZnO nanosheet and Ag_3PO_4 , suggesting a synergistic effect of surface oxygen vacancies and Ag_3PO_4 coupling.

© 2016 Elsevier B.V. All rights reserved.

1. Introduction

Semiconductor photocatalysis is a promising solution for many environment-related issues. Among various oxide semiconductor photocatalysts, ZnO has been intensively studied for degradation of organic pollutants due to its high quantum efficiency, nontoxic nature and low cost [1]. Unfortunately, intrinsic ZnO can only absorb ultraviolet light (5–7% of the total sunlight [2]) due to its wide band gap (3.2 eV) [3], which limits the photocatalytic efficiencies for practical applications. Research is now mainly focused on developing ZnO photocatalysts with high visible-light driven photo-activities via band-gap engineering. For example, doping of ZnO with various non-metal or transit-metal ions would make ZnO absorb photons of lower energy by generating narrower impurity

bands [4–6]. Compared with the conventional doping methods, introducing oxygen-related defects into ZnO could also enhance the visible-light absorption, by creating defect states lying under the conduction band (CB) of ZnO without introducing any impurities, providing an effective approach for visible-light photocatalysis [7,8]. Oxygen defect-rich ZnO was synthesized previously by chemical vapor deposition [9], plasma treatment [10], high-temperature annealing in atmospheres (e.g. H_2 , Ar) [11] and thermal decomposition of specific precursors (e.g. ZnO_2) [8]. Besides the above methods involving complicated procedures, there have been a few reports on the formation of ZnO nanostructures rich in oxygen defects by solution methods [12,13], which are more attractive because of mild conditions and low energy consumption. Therefore, it is highly desirable to develop simple and controllable solution synthesis of oxygen defect-rich ZnO nanostructures.

The visible-light photocatalytic process strongly depends on the surface properties of oxide photocatalysts [14,15]. Only the oxygen defects on the surface could serve as charge carrier traps where the charges transfer to the adsorbed species and prevent the photo-generated electron/hole (e^-/h^+) recombination while bulk defects

* Corresponding authors.

E-mail addresses: xianglan@mail.tsinghua.edu.cn (L. Xiang), sxk7@psu.edu (S. Komarneni).

¹ These two authors contributed equally to this work.

only act as charge carrier traps where e^-/h^+ recombine during photocatalytic process [16]. A correlation of photocatalytic activity with the concentration of surface defects has been observed for TiO_2 nanocrystals [14,17]. Therefore, construction of an oxide photocatalyst with high surface to volume ratio would be beneficial to increase the content of surface oxygen defects, which prevent the e^-/h^+ recombination and improve the visible-light photocatalytic activity. Although the relationship between oxygen defects and visible-light photocatalytic performance of ZnO nanostructures was widely investigated [18–21], little or no work addressed the surface area effects in visible-light photocatalysis. The surface areas of the ZnO nanostructures used in the above studies were generally small ($<10 \text{ m}^2/\text{g}$) or they were not reported. For example, the visible-light photocatalytic properties of ZnO tetrapods [18] and ZnO rods [12] were found to be induced by oxygen vacancies, however, the BET surface areas of the tetrapods and rods were only 2.2 and $7.2 \text{ m}^2/\text{g}$, respectively. Inspired by the above studies, the synthesis of ZnO nanostructures of high surface area and rich in oxygen defects could be an effective strategy to improve the visible-light photocatalytic performance.

In this work, we present a facile ultra-rapid solution synthesis of ZnO nanosheets with high BET surface area along with rich oxygen-vacancy defects. The BET surface area of ZnO was simply tuned by salt-addition, through an electrostatic-controlled self-assembly mechanism. Because of the rich oxygen-vacancies, the visible-light photocurrent responses and photocatalytic activities of the ZnO nanosheets were significantly improved compared to ZnO nanoparticles with few oxygen defects. Additionally, the hybridization of ZnO nanosheets with Ag_3PO_4 nanoparticles resulted in higher photocatalytic activities owing to the synergistic effect of surface oxygen vacancies and Ag_3PO_4 coupling. The mechanisms for enhanced visible-light photocatalytic performance and the charge transfer process were also discussed.

2. Experimental

2.1. Chemicals

Commercial chemicals of analytical grade and deionized water with a resistivity $>18 \text{ M}\Omega \text{ cm}^{-1}$ were used in all the experiments. Commercial ZnO nanoparticles ($>99.5\%$) were purchased from Sigma.

2.2. ZnO nanosheets photocatalysts

ZnO nanosheet-assemblies were synthesized from the super-saturated zinc-bearing alkaline solutions, using ZnO and NaOH as the starting chemicals. ZnO (1.253 g) and NaOH (4.000 g) were dissolved into water (10.0 mL) at room temperature to form a solution containing $1.54 \text{ mol L}^{-1} \text{ Zn}^{2+}$ and $10.00 \text{ mol L}^{-1} \text{ OH}^-$. 2 mL of the above solution was then diluted with 98 mL of water quickly at 60°C to form a supersaturated system. The solution became cloudy immediately after mixing and was kept stirring at 60°C for 1 min before centrifugation. The precipitates were then washed with deionized water and ethanol, and dried in an oven at 55°C for 24 h. The thickness and BET surface area of the ZnO nanosheets could be tuned by pre-dissolving of different amounts of Na_2SO_4 in water. The concentration of Na_2SO_4 in the synthesis solutions was adjusted in the range of $0\text{--}1.0 \text{ mol L}^{-1}$.

2.3. ZnO/ Ag_3PO_4 nanocomposites

The deposition of Ag_3PO_4 nanoparticles onto the ZnO nanosheets was carried out by an in-situ precipitation method. ZnO sample (0.15 g) was dispersed in 24 mL of $0.005 \text{ mol L}^{-1} \text{ AgNO}_3$ solution and sonicated for 30 min. Then 8 mL of 0.005 mol L^{-1}

Na_3PO_4 solution was added drop-wise to the above solution under vigorous magnetic stirring. The resulting yellow solution was kept stirring in dark for 2 h, then centrifuged, washed with deionized water and ethanol, followed by drying in an oven at 55°C for 12 h. For comparison, Ag_3PO_4 nanoparticles were prepared under the same conditions but without the addition of ZnO.

2.4. Characterization

The morphology and microstructure of the samples were examined with a field emission scanning electron microscope (FESEM, JSM 7401F, JEOL, Japan) and a high-resolution transmission electron microscope (HRTEM, JEM-2010, JEOL, Japan) equipped with energy-dispersive X-ray spectroscopy. Powder X-ray diffraction (XRD) was used for phase identification using an X-ray powder diffractometer (Bruker-AXS D8 Advance, Germany) with $\text{CuK}\alpha$ ($\lambda = 0.154178 \text{ nm}$) radiation. The Brunauer–Emmett–Teller (BET) surface areas of the products were determined using a nitrogen adsorption analyzer (Quadrasorb-S1, Quantachrome, USA) and the pore-size distribution was estimated by the Barrett–Joyner–Halenda method. The surface electric potential was measured with the zeta potential equipment (ZETAPALS, Brookhaven Instrument Corporation). Raman spectra were recorded using He-Ne laser excitation at 532 nm with a Horiba Jobin Yvon LabRAM HR800 Raman spectrometer. Photoluminescence (PL) spectra were measured at room temperature on a Hitachi F-7000 luminescence spectrometer using a Xe lamp with an excitation wavelength of 325 nm. Surface composition of the samples was characterized by X-ray photoelectron spectrometer (XPS, PHI-5300, PHI, USA). Electron-spin-resonance (ESR) measurements were performed on a JEOL-TE300 spectrometer operating at an X-band frequency of 9.4 GHz and UV–vis diffuse reflectance spectra were recorded on an Agilent UV-8453 spectrophotometer.

The photo-electrochemical experiments were performed in a three-electrode quartz cell with $0.1 \text{ mol L}^{-1} \text{ Na}_2\text{SO}_4$ electrolyte solution and recorded using an electrochemical system (CHI-660B, China). A xenon lamp equipped with an ultraviolet cutoff filter was employed as the visible light source ($\lambda > 420 \text{ nm}$; light intensity: 1 mW cm^{-2}). The working electrodes were prepared by drop-casting of the photocatalyst suspensions with a concentration of 10 mg mL^{-1} onto Ti foil and drying at 55°C for 12 h. Platinum wire and Ag/AgCl were used as the counter and reference electrode, respectively.

2.5. Photocatalytic activity measurements

The photocatalytic activities were evaluated at 25°C by the degradation of rhodamine B (RhB) under visible light irradiation from a 8 W Xe lamp equipped with an ultraviolet cutoff filter ($\lambda > 420 \text{ nm}$). In a typical run, 10 mg of the photocatalyst was dispersed in 50 mL of RhB aqueous solution (10 mg L^{-1}). Before irradiating, the above suspension was stirred in the dark for 30 min to achieve the adsorption-desorption equilibrium. The suspension was then illuminated under visible light, sampled at regular intervals of 10 or 15 min and centrifuged to remove the catalysts at 6000 rpm for 10 min. The UV–vis absorption spectra of the centrifuged solutions were measured by an Agilent UV-8453 spectrophotometer to determine the concentration of RhB. The initial concentration (C_0) was considered to be the RhB concentration after adsorption equilibrium.

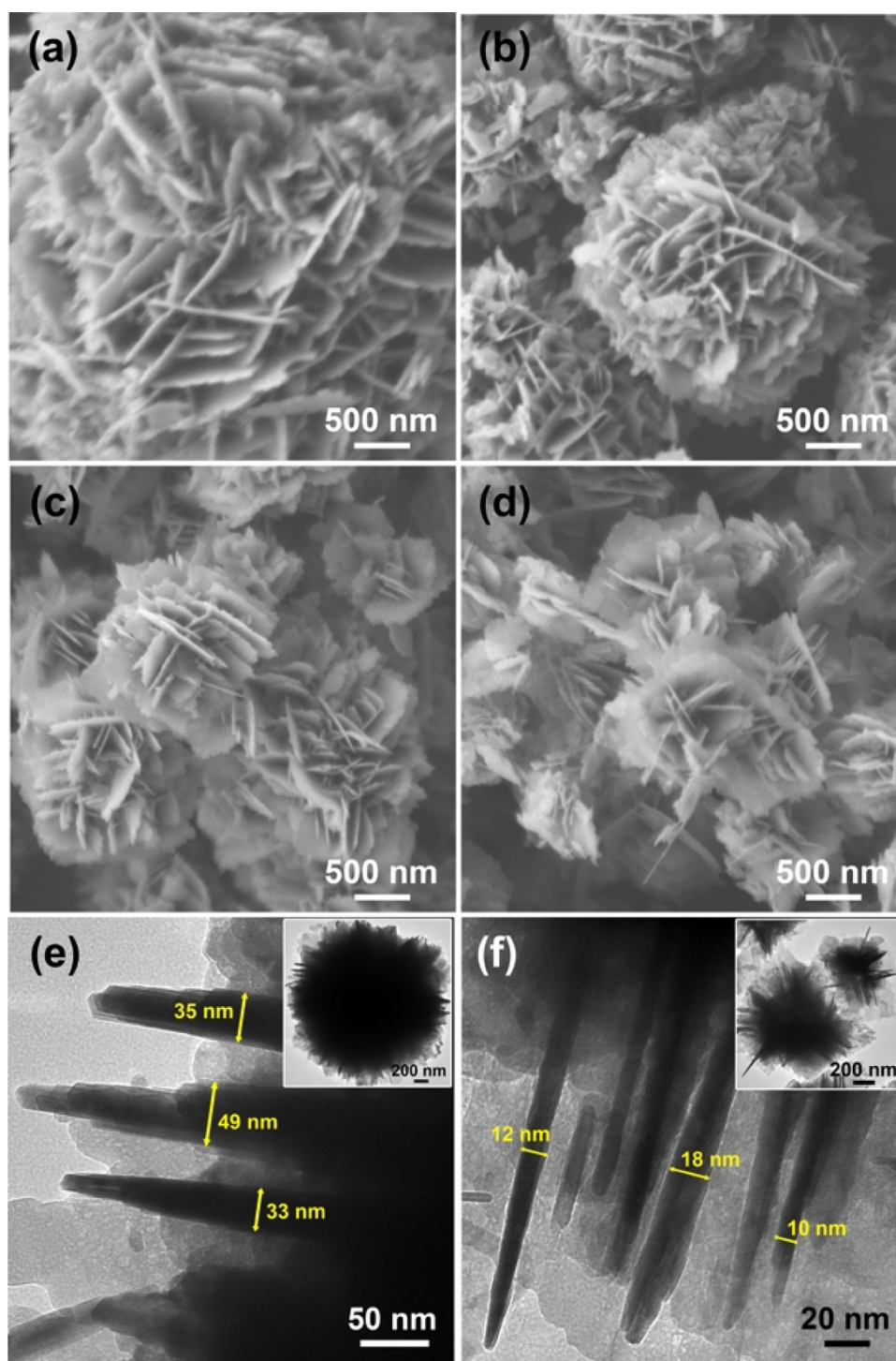


Fig. 1. SEM images (a–d) and TEM images (e, f) of the ZnO nanosheets formed in the presence of different Na_2SO_4 concentrations (mol L^{-1}): (a, e) 0; (b) 0.02; (c) 0.1; (d, f) 1.0.

3. Results and discussion

3.1. Formation of ZnO nanosheets with tunable BET surface areas

In this study, ZnO nanosheets with tunable thickness and BET surface area were controllably synthesized by a simple solution-based self-assembly approach using Na_2SO_4 as a growth modifier. The role of Na_2SO_4 concentration on the morphology of ZnO nanosheets was firstly examined by SEM and TEM. Fig. S1 and Fig. 1a–d show the low- and high-magnification SEM images, respectively of the ZnO samples formed in the

presence of 0–1.0 mol L^{-1} Na_2SO_4 . The SEM results demonstrate that the obtained ZnO displays a hierarchical porous network structure composed of intersecting nanosheets. With the increase of Na_2SO_4 concentration from 0 to 1.0 mol L^{-1} , the size of the nanosheet-assemblies decreased from 5 to 10 μm to 0.5–1 μm and the thickness of nanosheets gradually decreased from 30 to 50 nm to 10–15 nm. Some of the nanosheets formed at $[\text{Na}_2\text{SO}_4] = 1.0 \text{ mol L}^{-1}$ became semi-transparent due to their ultrathin nature. The density of the assembled nanosheets also decreased with increasing Na_2SO_4 concentration. At $[\text{Na}_2\text{SO}_4] = 1.0 \text{ mol L}^{-1}$, the nanosheets were loosely

assembled or even dis-assembled. The TEM observation (Fig. 1e and f) confirmed that the thickness of nanosheets decreased from 30 to 50 nm to 10–15 nm with increasing Na_2SO_4 concentration from 0 to 1.0 mol L^{-1} . The HRTEM images along with the Fast Fourier Transform (FFT) pattern (Fig. S2) revealed the preferential growth of the nanosheets along [001], with (100) planes as exposed surfaces. The XRD patterns (Fig. S3a) of all the four samples can be indexed to wurtzite ZnO (JCPDS 36–1451). The peak broadening and decreasing intensity of the (100) diffraction peaks (inset in Fig. S3b) indicated a decrease of the (100) crystallite size and poor crystallization of ZnO. The relative intensity ratio of (100) to (002) ($I_{(100)}/I_{(002)}$) gradually decreased from 1.81 to 0.55 with increasing Na_2SO_4 concentration from 0 to 1.0 mol L^{-1} , which implies that the growth of ZnO in (100) orientation was inhibited in the presence of Na_2SO_4 . These results are consistent with SEM and TEM observations, which showed a decreasing thickness of nanosheets with increasing Na_2SO_4 concentration.

The variation in nanosheets' size, thickness and density resulted in a variation of their BET surface areas and pore structures (Fig. 2a and b). The BET surface areas increased with increasing Na_2SO_4 concentration, i.e., the surface areas were 6.7, 18.1, 27.3 and $34.5 \text{ m}^2/\text{g}$ at Na_2SO_4 concentrations of 0, 0.02, 0.1 and 1.0 mol L^{-1} , respectively. The BET surface area of the nanosheets obtained here in 1.0 mol L^{-1} Na_2SO_4 was higher than many of those reported previously for ZnO nanosheets or even porous nanosheets [22–24]. The pore size distribution curves (Fig. 2b) revealed that the volume of the mesopores increased with increasing Na_2SO_4 concentration. In addition, the average size of the mesopores increased from ca. 15 nm to 30 nm, which is consistent with the SEM observation that showed the nanosheets being loosely assembled in the presence of concentrated Na_2SO_4 . The ZnO nanosheet-assemblies with higher surface area and more open pore structures may also find applications as adsorbents or catalyst supports in addition to photocatalysts. All the above results indicated that the growth and self-assembly of the ZnO nanosheets could be affected by Na_2SO_4 addition under the present synthesis conditions.

The effects of salt addition can be explained by an electrostatic-controlled growth and self-assembly mechanism. Insight into the time-dependent growth process of the ZnO nanosheets in the absence of Na_2SO_4 revealed that the nanosheets were formed by an ultra-rapid oriented attachment and self-assembly process, as revealed in Fig. S4. ZnO nanocrystals were immediately formed after dilution due to the high supersaturation (Fig. S4a), subsequently assembled into nanosheets by the two-dimensional oriented attachment process (Fig. S4b) with many nanocrystal-boundaries still remaining in the nanosheets (Fig. S4c), and further assembled into well-defined nanosheet-assemblies (Fig. S4d). The whole self-assembly process was superfast and could be completed within only 1 min. The driving forces that assemble nanocrystals into nanosheets were generally attributed to anisotropic hydrophobic attraction or electrostatic interactions derived from dipole moments and surface charges [25,26]. In the present case, hydrophobic attraction could be ruled out since no organic template/surfactant was added. Therefore, the surface charge of the nanocrystals may affect the oriented attachment process. Fig. 2c shows the variation of zeta potential of the ZnO nanosheets with Na_2SO_4 concentration. The zeta potential of the ZnO nanosheets dropped from -12.1 eV to -67.5 eV with increasing Na_2SO_4 concentration from 0 to 1.0 mol L^{-1} . The zeta potentials indicate that ZnO became more negatively charged in the presence of Na_2SO_4 , thus the attachment and self-assembly of the initial nanocrystals were hindered due to the electrostatic repulsion, which led to the formation of thinner and smaller nanosheets with looser packing. Such effects could also be observed in the presence of other salts such as NaNO_3 , Na_2CO_3 and NaCl , as displayed in the SEM images in Fig. S5. The summarized data of zeta potentials and BET surface

areas of the ZnO nanosheets under different conditions are shown in Fig. 2d. The clear correlation between BET surface areas and surface charges suggested that the growth and self-assembly of ZnO nanosheets were controlled by electrostatic process. The effects of salt addition on the attachment behavior of ZnO nanocrystals may be explained by Derjaguin Landau Verwey Overbeek (DLVO) theory, in which the main force between the nanocrystals were electrical double layer repulsion derived from the ion adsorption layers around the nanocrystals [27]. In the present case, the effect of Na_2SO_4 addition was more significant compared to other salts, which could be attributed to the preferential adsorption of SO_4^{2-} onto the (100) planes of ZnO, as revealed in our previous work [28]. Such electrostatic-controlled synthesis strategy has also been employed in the hydrothermal growth of ZnO nanowires with tunable aspect ratios [29]. However, the electrostatic-mediated self-assembly of ZnO nanocrystals into three-dimensional hierarchical structures in a controlled manner has not been reported yet. The presently developed method may provide an alternative route to control the BET surface areas of solution-processed inorganic nanostructures. Moreover, the adsorbed inorganic ions in the current work (see EDS spectra in Fig. S6) could be completely removed by washing unlike many organic surfactants used in other works as growth modifiers [30,31], which may inhibit the active sites of the photocatalysts.

3.2. Identification of oxygen defects in ZnO nanosheets

As shown above, ZnO nanosheets were formed from highly-supersaturated solution by an ultra-rapid self-assembly process [32]. Such a non-equilibrium synthesis process was generally considered to lead to the generation of a high-concentration of defects [33–35]. Multiple techniques were employed to identify the defect states of the ZnO nanosheets with different BET surface areas formed in 0 and 1 mol L^{-1} Na_2SO_4 solutions, which were denoted as ZNS-1 and ZNS-4, respectively. Commercial ZnO nanoparticles with an average diameter of 20 nm and a BET surface area of $43.4 \text{ m}^2/\text{g}$ (denoted as ZnO NPs) were used as a reference (Fig. S7). Fig. 3a shows the Raman spectra of the different samples. Little difference was observed among the peaks located at 333 cm^{-1} , 380 cm^{-1} and 439 cm^{-1} , which corresponded to $2\text{E}_2(\text{low})$, $\text{A}_1(\text{TO})$ and $\text{E}_2(\text{high})$ modes of ZnO, respectively. The $\text{E}_1(\text{LO})$ modes (located at 582 cm^{-1}) of the samples emerged as a red shift compared with that of the bulk ZnO (591 cm^{-1}), which may be assigned to the oxygen deficiencies such as oxygen vacancies (V_O) in ZnO [36]. The order of the intensities of $\text{E}_1(\text{LO})$ mode was $\text{ZNS-4} > \text{ZNS-1} > \text{ZnO NPs}$ (inset in Fig. 3a), indicating the much higher concentration of oxygen-related defects in ZnO nanosheets compared to ZnO nanoparticles. Fig. 3b shows the room temperature PL spectra of the samples. The ZnO NPs displayed an ultraviolet (UV) emission peak with maximal intensity at around 384 nm, which was due to the excitonic recombination of the photogenerated holes in the valence band (VB) and the electrons in the conduction band (CB) [37]. However, the characteristic UV emission was not clearly distinguished in the as-prepared nanosheets, indicating that high concentrations of defects were introduced into the samples. The multi-peak bands of the nanosheets in the range of 400–480 nm were generally ascribed to the recombination of the electrons from the shallow level donor of zinc interstitials (Zn_i) and a series of extended Zn_i states to holes in the valence band. In the green-yellow region, a very weak green emission centered at about 500 nm was observed for ZnO NPs, while the nanosheets exhibited intensive green-yellow emission centered at 550 nm, which could be divided into two peaks, including the green emission at $\sim 520 \text{ nm}$ originated from singly charged oxygen vacancies ($\text{V}_\text{O}^\bullet$) and the yellow one at $\sim 580 \text{ nm}$ originated from doubly charged oxygen vacancies ($\text{V}_\text{O}^{\bullet\bullet}$) [35,38].

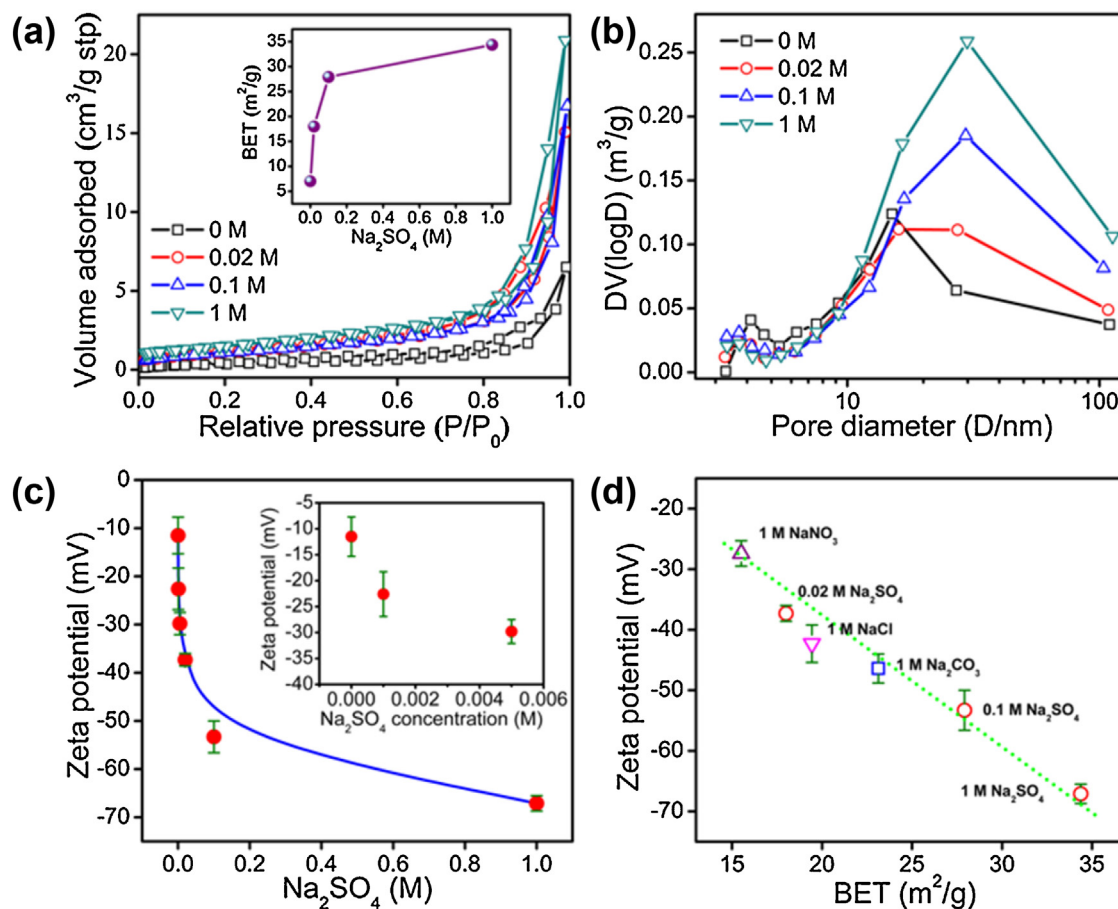


Fig. 2. N_2 adsorption-desorption isotherms (a), pore size distributions (b) of the ZnO nanosheets formed in the presence of Na_2SO_4 with different concentrations, inset in Fig. 2a is the variation of specific surface area of the samples with Na_2SO_4 concentration; (c) variation of zeta potential of the ZnO nanosheets with Na_2SO_4 concentration; (d) summarized zeta potentials and specific surface areas of the samples formed under different conditions (the dashed line serves as a guide line).

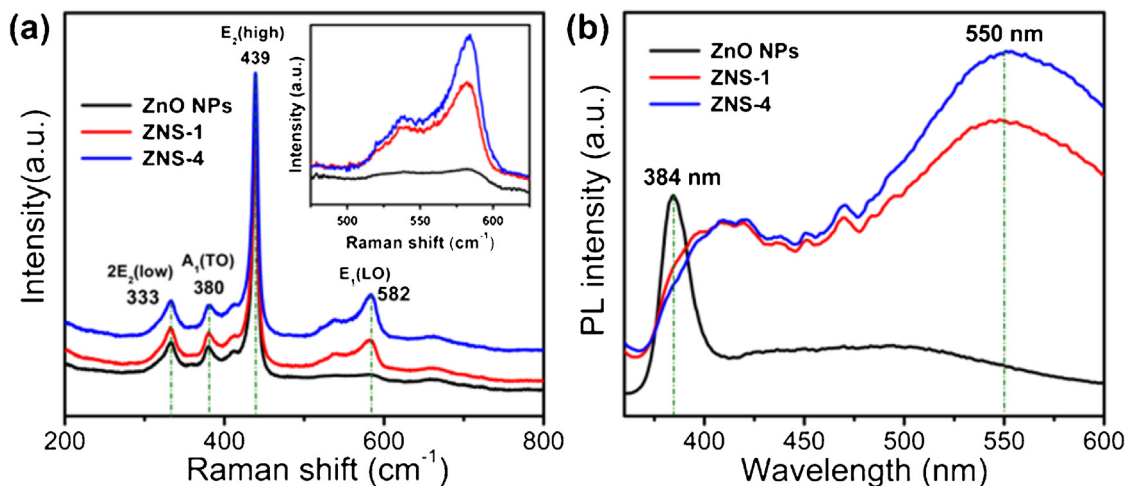


Fig. 3. Raman spectra (a) and room-temperature PL spectra (b) of ZNS-1, ZNS-4 and ZnO nanoparticles. Inset in Fig. 3a is the enlarged $E_1(\text{LO})$ modes.

Since Raman and PL spectra give information on both bulk and surface oxygen defects, XPS and ESR spectra were employed to further characterize the surface properties of the ZnO samples. Fig. 4a shows the high-resolution O1s spectra of the three samples. Two species centered at the binding energies of ca. 530.2–530.3 eV and 531.6–531.7 eV were denoted as O1 and O2, respectively. The species of O1 were originated from the lattice oxygen anions (O^{2-}) in wurtzite structure, while the species of O2 belonged to the O_x^-

ions (O^- and O_2^-) in the oxygen-deficient regions caused by V_O on ZnO surface [39]. The ratios of O2 species on the surface of ZnO NPs, ZNS-1 and ZNS-4 were 13.9, 46.8 and 54.1%, respectively, indicating that the as-prepared ZnO nanosheets had a high concentration of surface oxygen vacancies. Fig. 4b shows the ESR spectra of the three samples. The signal with g -factor = 2.01 is close to the free-electron value ($g \sim 2.0023$), which was previously attributed to an unpaired electron trapped on a surface oxygen vacancy site

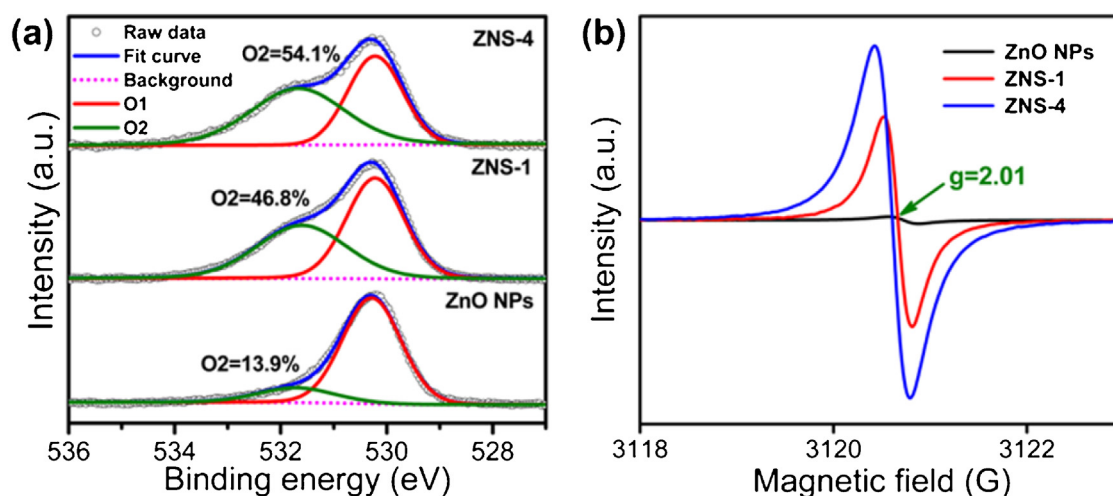


Fig. 4. High-resolution O1s XPS spectra (a) and ESR spectra (b) of ZNS-1, ZNS-4 and ZnO NPs.

[40]. This is because the surface oxygen vacancy is prone to adsorb atmospheric O_2 molecules and form $\bullet O_2^-$ to generate such a signal [41]. The nanosheets had a much higher ESR signal at $g=2.01$ in contrast to ZnO NPs. All the results discussed above confirmed the existence of a high concentration of oxygen vacancies in the as-prepared ZnO nanosheets. Moreover, a higher concentration of surface oxygen vacancies was observed for ZNS-4 compared with ZNS-1 owing to its higher surface to volume ratio, suggesting that increasing the BET surface area of ZnO was an effective method to enrich its surface oxygen vacancies, which are useful to the visible-light photocatalytic process.

The optical properties of ZNS-1, ZNS-4 and ZnO NPs were examined by UV–vis diffuse reflectance spectroscopy to evaluate the effect of oxygen vacancy on the absorption characteristics, as shown in Fig. 5a. ZnO NPs only absorbed the light with $\lambda < 420$ nm owing to its intrinsic wide band gap, while the absorption curves of as-prepared ZnO nanosheets exhibited a red shift to longer wavelength compared to the ZnO NPs reference while the ZNS-4 sample showed the highest absorption in visible-light region ($\lambda > 420$ nm). The large absorption tail occurring in the visible-light regions of the ZnO nanosheets was attributed to the rich oxygen vacancies, which generated a defect-isolated state of about 0.8 eV below the conduction band of ZnO, promoting the visible-light absorption [42,43]. Therefore, we can conclude that the visible-light absorption of ZnO could be effectively improved by introducing oxygen vacancies, and the absorption capacity was related to the concentration of oxygen vacancies.

The photocurrent responses of the samples were tested on a photoelectrochemical test device to further investigate the activity of ZnO in visible-light region. Fig. 5b shows the photocurrent responses of ZNS-1, ZNS-4 and ZnO NPs as a function of time with visible light-on and -off cycles. ZnO NPs electrode showed very weak photocurrent response under visible-light irradiation ($\lambda > 420$ nm), while the as-prepared ZNS-1 and ZNS-4 samples of ZnO nanosheets showed much larger photocurrent responses, which are about 9 and 13 times higher, respectively than that of ZnO NPs (Fig. 5b). This suggests that ZNS-1 and ZNS-4 samples are expected to have enhanced generation and separation efficiency of photogenerated carriers under visible-light. The highest photocurrent of ZNS-4 could be attributed to the highest concentration of surface oxygen vacancies derived from the increased surface to volume ratio, which may lead to the improved visible-light absorption and surface oxygen-vacancy-mediated electrons/holes generation and separation [16].

3.3. Photocatalytic performance and mechanisms

The photocatalytic performances of ZNS-1, ZNS-4 and ZnO NPs were evaluated by degradation of RhB under visible-light irradiation ($\lambda > 420$ nm). As shown in Fig. 6a, the ZnO NPs reference shows very low activity in photodegradation due to its poor visible-light absorption capacity, and only about 9.4% of RhB was degraded after 90 min of irradiation, even though it has a larger BET surface area ($43.4 \text{ m}^2/\text{g}$). In contrast, the degradation ratio of RhB was 35.3 and 55.1% for ZNS-1 and ZNS-4 after 90 min, respectively. The enhanced visible-light photocatalytic activity could be explained by the oxygen vacancy-enhanced visible-light absorption and charge separation. When defect-rich ZnO nanosheets were under visible-light illumination, the electrons in the VB could be excited to the oxygen vacancy induced defect energy level due to the lowered energy difference ($\Delta E = 2.4 \text{ eV}$). The holes left behind in the VB can react with water adhering to the surfaces of ZnO to form hydroxyl radicals ($\bullet OH$) which can result in the oxidation of the organic dye, while the photogenerated electrons could get trapped in the surface oxygen defects working as electron acceptors, leading to the occurrence of the redox reactions [19]. Therefore, the surface oxygen defects not only improve the visible-light absorption of ZnO, but also act as the active sites for photocatalytic reactions, which facilitated the e^-/h^+ separation and prevented their recombination. Therefore, the ZNS-4 sample with highest concentration of surface oxygen vacancies exhibited significantly enhanced visible-light photocatalytic activity, as expected.

Sheet-like structures with high surface areas can easily combine with other functional particles through the two faces of the sheets, which is another approach to further enhance the visible-light photocatalytic activity [23]. Although the activation of ZnO under visible-light irradiation by hybridization with various materials including noble metal nanoparticles, narrow band-gap semiconductors and carbon nanomaterials [44–46], have been widely reported, there were only a few reports related to the synergistic effect of surface oxygen defects of ZnO by hybridizing with a second phase. For example, enhanced photocatalytic activities were achieved by hybridization of oxygen defect-rich ZnO nanostructure with Ag nanoparticles [21] or graphene nanosheets [16]. However, such synergistic effect has not been reported yet for defect-rich ZnO coupled with other narrow band-gap semiconductors. Herein, therefore, we also investigated the synergistic effect of surface oxygen defects by combining Ag_3PO_4 as a second phase, i.e., ZnO/ Ag_3PO_4 nanocomposites as a case study. Ag_3PO_4 nanoparticles were deposited onto the surfaces of ZnO nanosheets by a

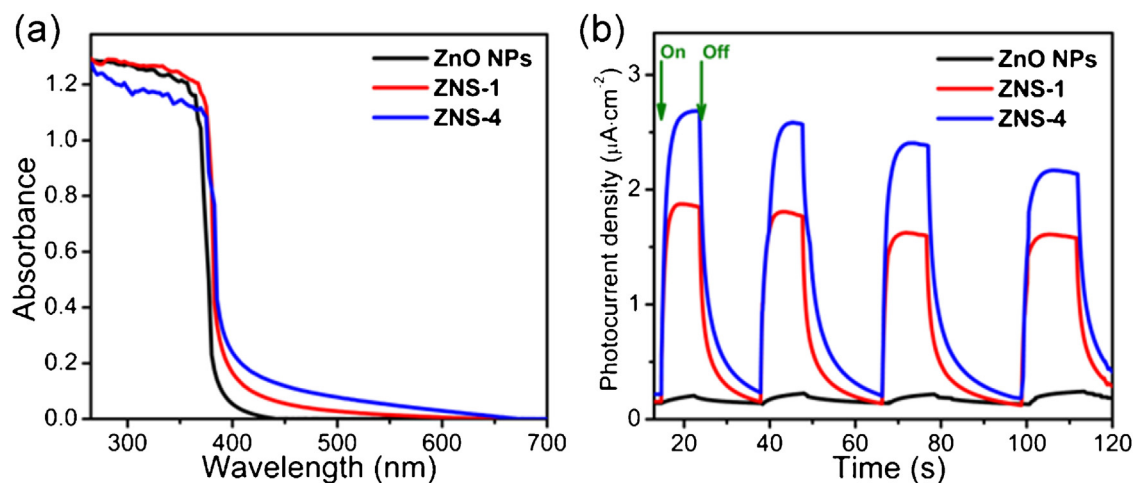


Fig. 5. (a) UV-vis diffuse reflectance spectra of ZNS-1, ZNS-4 and ZnO NPs; (b) photocurrent response of the ZNS-1, ZNS-4 and ZnO NPs electrodes under the irradiation of visible-light ($\lambda > 420\text{ nm}$).

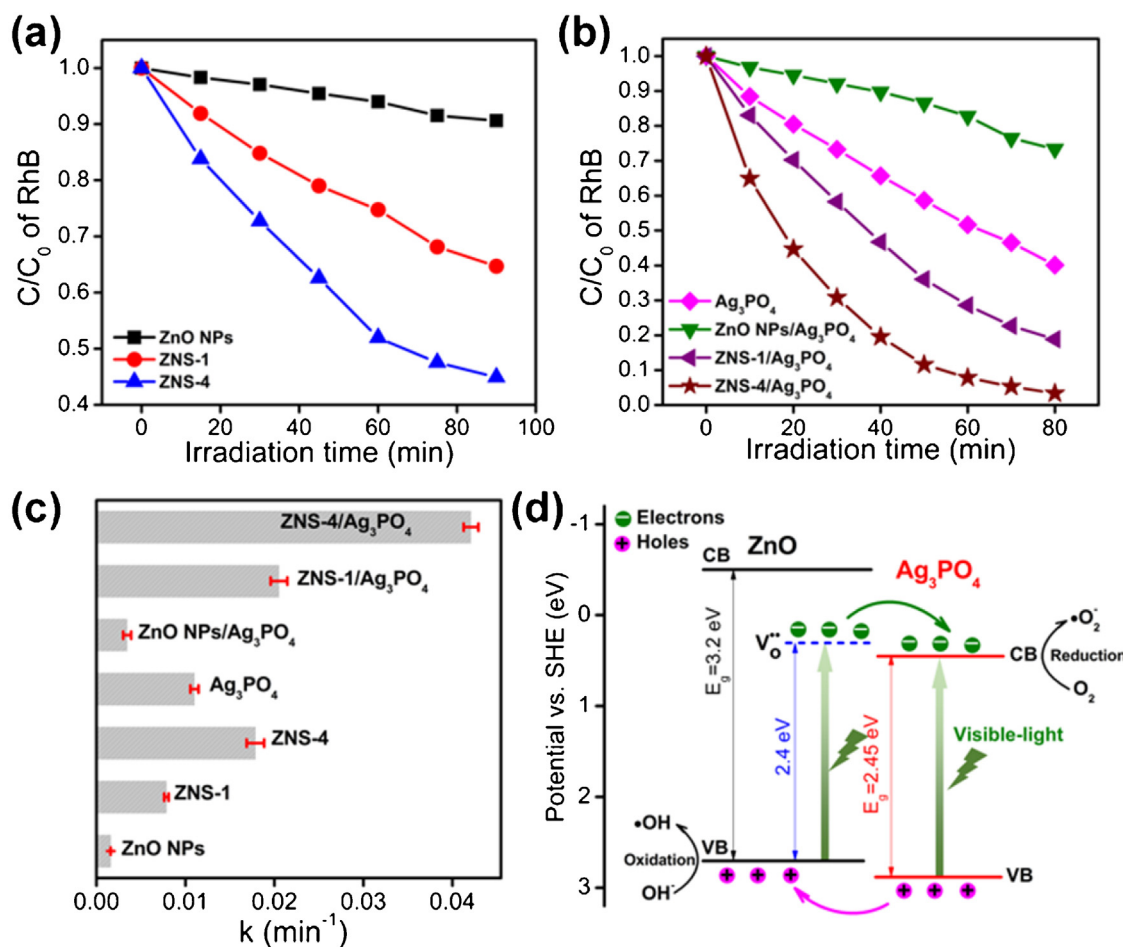


Fig. 6. (a, b) Photocatalytic degradation of RhB under visible-light irradiation in the presence of different ZnO or ZnO/ Ag_3PO_4 nanocomposite samples; (c) apparent rate constants (k , min^{-1}) of the tested samples determined by the pseudo first-order kinetic equation; (d) schematic illustration of the band structure and charge-transfer process of oxygen defect-rich ZnO coupled with Ag_3PO_4 under visible-light illumination.

simple in-situ precipitation method. Representative XRD pattern of the as-obtained ZNS-4/ Ag_3PO_4 nanocomposite confirmed the coexistence of ZnO and Ag_3PO_4 phases (Fig. S8a). The TEM and HRTEM images (Figs. S8b and c) revealed that Ag_3PO_4 nanoparticles with diameters of 5–30 nm were coated onto the surfaces of ZnO nanosheets. UV-vis spectrum (Fig. S8d) indicated that

the absorption in the visible-light region of the ZNS-4/ Ag_3PO_4 nanocomposite increased significantly due to the narrow band gap of Ag_3PO_4 (2.45 eV), which can absorb light with a wavelength of less than 503 nm [47]. The increased visible-light absorption of the nanocomposites led to the enhancement of the visible-light photocatalytic activities, as shown in Fig. 6b. The apparent rate

constants of the tested samples were determined by the pseudo first-order kinetic equation (Fig. S9) and displayed in Fig. 6c and these results clearly demonstrate the photocatalytic activity order of the samples. For ZNS-1/Ag₃PO₄ and ZNS-4/Ag₃PO₄ samples, the photodegradation ratio of RhB increased to 81.1 and 96.6% after 80 min of irradiation. The determined rate constants for the above two samples were 0.0205 and 0.0421 min⁻¹, respectively, which are higher than that of either ZnO nanosheets or Ag₃PO₄ samples, indicating the enhanced visible-light photocatalytic activity of the ZnO/Ag₃PO₄ nanocomposites. However, the ZnO NPs/Ag₃PO₄ sample showed much lower activity compared to solely Ag₃PO₄ even though the total weight of the photocatalyst was kept constant (10 mg), due to the low loading amount of Ag₃PO₄ (~10.0 wt%) on ZnO NPs with few defects, which are not active in visible light. These results implied that surface oxygen defects of ZnO played a critical role of in the photocatalytic performance of the nanocomposites. Therefore, the enhanced visible-light photocatalytic activity of ZnO nanosheets/Ag₃PO₄ nanocomposites could be attributed to not only the increased visible-light absorption, but also the synergistic effect of surface oxygen vacancies and Ag₃PO₄ coupling. The VB and CB positions of Ag₃PO₄ vs. NHE (normal hydrogen electrode) are 2.9 and 0.45 eV [48], lower than the VB (2.6 eV) and oxygen defects energy level (0.2 eV) of ZnO, respectively, thus an energy level matching is established between Ag₃PO₄ and ZnO with rich oxygen-vacancies, as illustrated in Fig. 6d. Under visible-light illumination, the electrons in VB of ZnO and Ag₃PO₄ could be excited to the oxygen-vacancy defect energy level of ZnO and CB of Ag₃PO₄, respectively, thus leading to highly increased visible-light absorption. On the other hand, the excited electrons in the defect energy level of ZnO would transfer to the CB of Ag₃PO₄, and the holes in the VB of Ag₃PO₄ would transfer to the VB of the ZnO. Such spatial separation of the photogenerated electrons/holes within the nanocomposite by a direct Z-scheme mechanism significantly reduced the electron-hole recombination ratio, which promoted the subsequent redox reactions leading to a much higher visible-light photocatalytic performance of the nanocomposites [49,50]. These results suggest that ZnO nanostructures with rich oxygen vacancies are more suitable for constructing functional nanocomposites for visible-light photocatalysis applications.

4. Conclusion

In summary, ZnO nanosheets with high surface area and rich oxygen vacancies were synthesized via a salt-assisted ultrarapid solution method. An electrostatic-controlled self-assembly mechanism was proposed for the effects of salt addition. The results obtained by Raman, PL, XPS and ESR analyses indicated that the as-prepared nanosheets had much higher concentration of oxygen vacancies compared to ZnO nanoparticles. The increased BET surface areas achieved here contributed to the increase of surface oxygen vacancies, which could improve the visible-light absorption and act as active sites for photocatalytic reactions, leading to the enhancement of photocurrent and photocatalytic activities of the ZnO nanosheets under visible-light illumination. Hybridization of ZnO nanosheets with Ag₃PO₄ nanoparticles further improved the visible-light photocatalytic activity, which was attributed to the efficient charge transfer between ZnO and Ag₃PO₄ through energy level matching, suggesting a synergistic effect of surface oxygen vacancies and Ag₃PO₄ coupling.

Acknowledgements

This work was financially supported by the National Science Foundation of China (Nos. 51174125, 51234003 and 51374138), National Key Technology Research and Development Program of

China (2013BAC14B02). Jing Wang is grateful for the scholarship from China Scholarship Council (No. 201506210232).

Appendix A. Supplementary data

Supplementary data associated with this article can be found, in the online version, at <http://dx.doi.org/10.1016/j.apcatb.2016.03.040>.

References

- [1] S. Sakthivel, B. Neppolian, M. Shankar, B. Arabinthoo, M. Palanichamy, V. Murugesan, *Sol. Energy Mater. Sol. Cells* 77 (2003) 65–82.
- [2] T. Bak, J. Nowotny, M. Rekas, C. Sorrell, *Int. J. Hydrogen Energy* 27 (2002) 991–1022.
- [3] M. Miyauchi, A. Nakajima, T. Watanabe, K. Hashimoto, *Chem. Mater.* 14 (2002) 2812–2816.
- [4] J.C. Sin, S.M. Lam, I. Satoshi, K.T. Lee, A.R. Mohamed, *Appl. Catal. B: Environ.* 148 (2014) 258–268.
- [5] Y. Lu, Y. Lin, D. Wang, L. Wang, T. Xie, T. Jiang, *Nano Res.* 4 (2011) 1144–1152.
- [6] S. Liu, C. Li, J. Yu, Q. Xiang, *CrystEngComm* 13 (2011) 2533–2541.
- [7] S. Rehman, R. Ullah, A. Butt, N. Gohar, J. Hazard. Mater. 170 (2009) 560–569.
- [8] J. Wang, Z. Wang, B. Huang, Y. Ma, Y. Liu, X. Qin, X. Zhang, Y. Dai, *ACS Appl. Mater. Interfaces* 4 (2012) 4024–4030.
- [9] X. Liu, X. Wu, H. Cao, R. Chang, *J. Appl. Phys.* 95 (2004) 3141–3147.
- [10] F. Liu, Y.H. Leung, A.B. Djurišić, A.M.C. Ng, W.K. Chan, K.L. Ng, K.S. Wong, C. Liao, K. Shih, C. Surya, *J. Phys. Chem. C* 118 (2014) 22760–22767.
- [11] K. Tam, C. Cheung, Y. Leung, A.B. Djurišić, C. Ling, C. Beling, S. Fung, W. Kwok, W. Chan, D. Phillips, *J. Phys. Chem. B* 110 (2006) 20865–20871.
- [12] S. Mukhopadhyay, P.P. Das, S. Maity, P. Ghosh, P.S. Devi, *Appl. Catal. B: Environ.* 165 (2015) 128–138.
- [13] H.L. Guo, Q. Zhu, X.L. Wu, Y.F. Jiang, X. Xie, A.W. Xu, *Nanoscale* 7 (2015) 7216–7223.
- [14] E. Grabowska, J.W. Sobczak, M. Gazda, A. Zaleska, *Appl. Catal. B: Environ.* 117 (2012) 351–359.
- [15] X. Chen, L. Liu, Y.Y. Peter, S.S. Mao, *Science* 331 (2011) 746–750.
- [16] X. Bai, L. Wang, R. Zong, Y. Lv, Y. Sun, Y. Zhu, *Langmuir* 29 (2013) 3097–3105.
- [17] M. Kong, Y. Li, X. Chen, T. Tian, P. Fang, F. Zheng, X. Zhao, *J. Am. Chem. Soc.* 133 (2011) 16414–16417.
- [18] M.Y. Guo, A.M.C. Ng, F. Liu, A.B. Djurišić, W.K. Chan, H. Su, K.S. Wong, *J. Phys. Chem. C* 115 (2011) 11095–11101.
- [19] J. Wang, P. Liu, X. Fu, Z. Li, W. Han, X. Wang, *Langmuir* 25 (2008) 1218–1223.
- [20] G. Li, T. Hu, G. Pan, T. Yan, X. Gao, H. Zhu, *J. Phys. Chem. C* 112 (2008) 11859–11864.
- [21] Y. Zheng, L. Zheng, Y. Zhan, X. Lin, Q. Zheng, K. Wei, *Inorg. Chem.* 46 (2007) 6980–6986.
- [22] G.-X. Tong, F.F. Du, Y. Liang, Q. Hu, R.N. Wu, J.G. Guan, X. Hu, *J. Mater. Chem. B* 1 (2013) 454–463.
- [23] Y. Hong, C. Tian, B. Jiang, A. Wu, Q. Zhang, G. Tian, H. Fu, *J. Mater. Chem. A* 1 (2013) 5700–5708.
- [24] H. Lu, S. Wang, L. Zhao, J. Li, B. Dong, Z. Xu, *J. Mater. Chem.* 21 (2011) 4228–4234.
- [25] Z. Zhang, Z. Tang, N.A. Kotov, S.C. Glotzer, *Nano Lett.* 7 (2007) 1670–1675.
- [26] Z. Tang, Z. Zhang, Y. Wang, S.C. Glotzer, N.A. Kotov, *Science* 314 (2006) 274–278.
- [27] S.W. Bian, I.A. Mudunkotuwa, T. Rupasinghe, V.H. Grassian, *Langmuir* 27 (2011) 6059–6068.
- [28] L. Yang, J. Wang, L. Xiang, *Particuology* 19 (2015) 113–117.
- [29] J. Joo, B.Y. Chow, M. Prakash, E.S. Boyden, J.M. Jacobson, *Nat. Mater.* 10 (2011) 596–601.
- [30] E.O. Oseghie, S. Maddila, P.G. Ndungu, S.B. Jonnalagadda, *Appl. Catal. B: Environ.* 176 (2015) 288–297.
- [31] J. Li, G. Lu, Y. Wang, Y. Guo, Y. Guo, *J. Colloid Interface Sci.* 377 (2012) 191–196.
- [32] J. Wang, S. Hou, L. Zhang, J. Chen, L. Xiang, *CrystEngComm* 16 (2014) 7115–7123.
- [33] I.Y. Bu, *Ceram. Int.* 39 (2013) 1189–1194.
- [34] M.A. Mahmood, S. Baruah, J. Dutta, *Mater. Chem. Phys.* 130 (2011) 531–535.
- [35] H. Zeng, G. Duan, Y. Li, S. Yang, X. Xu, W. Cai, *Adv. Funct. Mater.* 20 (2010) 561–572.
- [36] Ü Özgür, Y.I. Alivov, C. Liu, A. Teke, M. Reshchikov, S. Doğan, V. Avrutin, S.-J. Cho, H. Morkoc, *J. Appl. Phys.* 98 (2005) 041301.
- [37] Y. Chen, D. Bagnall, H.J. Koh, K.T. Park, K. Hiraga, Z. Zhu, T. Yao, *J. Appl. Phys.* 84 (1998) 3912–3918.
- [38] K. Vanheusden, C. Seager, W.T. Warren, D. Tallant, J. Voigt, *Appl. Phys. Lett.* 68 (1996) 403–405.
- [39] K. Kotsis, V. Staemmler, *Phys. Chem. Chem. Phys.* 8 (2006) 1490–1498.
- [40] I. Nakamura, N. Negishi, S. Kutsuna, T. Ihara, S. Sugihara, K. Takeuchi, *J. Mol. Catal. A: Chem.* 161 (2000) 205–212.
- [41] X. Zou, J. Liu, J. Su, F. Zuo, J. Chen, P. Feng, *Chem. Eur. J.* 19 (2013) 2866–2873.
- [42] Y. Zheng, C. Chen, Y. Zhan, X. Lin, Q. Zheng, K. Wei, J. Zhu, Y. Zhu, *Inorg. Chem.* 46 (2007) 6675–6682.
- [43] A.B. Djurišić, Y.H. Leung, *Small* 2 (2006) 944–961.

- [44] T. Xu, L. Zhang, H. Cheng, Y. Zhu, *Appl. Catal. B: Environ.* 101 (2011) 382–387.
- [45] P. Kundu, P.A. Deshpande, G. Madras, N. Ravishankar, *J. Mater. Chem.* 21 (2011) 4209–4216.
- [46] Q. Wang, B. Geng, S. Wang, *Environ. Sci. Technol.* 43 (2009) 8968–8973.
- [47] W. Yao, B. Zhang, C. Huang, C. Ma, X. Song, Q. Xu, *J. Mater. Chem.* 22 (2012) 4050–4055.
- [48] Z. Yi, J. Ye, N. Kikugawa, T. Kako, S. Ouyang, H. Stuart-Williams, H. Yang, J. Cao, W. Luo, Z. Li, *Nat. Mater.* 9 (2010) 559–564.
- [49] F. Peng, Q. Zhou, D. Zhang, C. Lu, Y. Ni, J. Kou, J. Wang, Z. Xu, *Appl. Catal. B: Environ.* 165 (2015) 419–427.
- [50] S. Liu, M.Q. Yang, Z.R. Tang, Y.J. Xu, *Nanoscale* 6 (2014) 7193–7198.